

Heterogeneous Seeded Growth: Synthesis and Characterization of Bifunctional Fe₃O₄/ZnO Core/Shell Nanocrystals

Weesiong Chiu,^{*,†} Poisim Khiew,[†] Michael Cloke,[†] Dino Isa,[†] Hongngsee Lim,[†] Thiankhoo Tan,[†] Nayming Huang,[‡] Shahidan Radiman,[§] Roslan Abd-Shukor,[§] M. Azmi Abd. Hamid,[§] and Chinhua Chia[§]

Department of Chemical Engineering, Faculty of Engineering, University of Nottingham Malaysia Campus, Broga Road, 43500, Semenyih, Selangor Darul Ehsan, Malaysia, School of Applied Physics, Faculty of Science & Technology (UKM), Universiti Kebangsaan Malaysia, 43600 Bangi, Selangor Darul Ehsan, Malaysia, Solid State Physics Research Laboratory, Department of Physics, Faculty of Science, University of Malaya, 50603 Kuala Lumpur, Malaysia

Received: January 28, 2010; Revised Manuscript Received: March 25, 2010

In the present study, Fe₃O₄/ZnO core/shell nanocrystals (NCs) are synthesized via seed-mediated growth approach in nonhydrolytic condition. The controlling process of thermal pyrolysis of zinc acetate (ZnAc) renders a condition to overgrow ZnO layer on the surface of Fe₃O₄ NCs (seeds). The transmission electron microscope (TEM) micrograph shows that Fe₃O₄/ZnO NCs are spherical in shape, highly monodispersed, and exhibiting responding shell thickness by varying the mole ratio of seed to shell precursor. The X-ray powder diffraction patterns (XRD) for Fe₃O₄/ZnO NCs reveal the coexistence of both Fe₃O₄ and ZnO crystal structures, which the patterns can be well indexed with the standard powder diffraction patterns of both materials. The NCs exhibit superparamagnetism corresponding to an external magnet field provided by vibrating sample magnetometer (VSM) and show red-shift phenomenon under UV excitation at room temperature. The NCs are magnetically separable upon application of 0.6 T magnet, which shows that high potentiality of the NCs to be used as regenerable catalyst material.

Introduction

For last two decades, the interest in developing materials has culminated especially in the preparation of high quality materials with enhanced functionality. The driven force for the preparation of these so-called “smart materials” had the promise as first prototypes in various applications such as catalysis,^{1–4} biomedical engineering,⁵ and sensing.^{6,7} Recently, tremendous advances in the solution-phase colloidal chemistry approach have greatly enhanced the processability of various kinds of nanomaterials with multifunctional properties.^{2,8,9} As a result, the developments of these “smart materials” have been increasingly oriented among scientific communities and various breakthrough discoveries have been reported.

For example, Alivisatos et al. reported on the inorganic core–shell II–VI semiconductor nanocrystals (NCs), which were developed through scrupulously engineered band gap patterning.^{10,11} In contrast to their single-component counterparts, these nanocomposites are found to exhibit prolonged photoluminescence lifetimes (≈50%) and excellent stability against photochemical oxidation.¹² In additional, this nanofeature also enables tuning of the light emission that displays narrow linewidths and high quantum yields across the visible and near-infrared part of the spectrum (500–1050 nm). This achievement has crucially benefited the biolabeling application by introducing new possibilities for ultrasensitive and multiplexed imaging of molecular targets in vivo.¹³ On the other hand, Seshadri et al. had successfully in synthesizing CoFe₂O₄/MnO core–shell

magnetic NCs that exhibit novel magnetic properties with exchange-biased architectures.¹⁴ As a comparison to pure CoFe₂O₄ NCs, these core–shell NCs show enhancements in saturation magnetization due to the existence of exchange biasing at the ferrimagnetic/antiferromagnetic interface that hold the potential to be used as read-heads in high-density magnetic storage media.

However, all the examples mentioned above are merely composed of a single property (either optical or magnetic property alone) after enhancement of the preceding rather than a combination of these two properties. In fact, the novel bifunctional nanomaterials that exhibit magnetic-optical properties are good candidates for “bioassays” through harnessing of the optical properties as “markers” and magnetic properties as “vehicles”. Few interesting reports about this class of “smart materials”, which have been reported recently, have tremendously overwhelmed the scientific communities as these major breakthroughs could overcome the limitation of the preceding inorganic materials that only exhibit either magnetic or optical properties alone. For instance, Bawendi et al. had successfully synthesized magnetic-fluorescent microspheres through incorporating maghemite (γ-Fe₂O₃) nanoparticles and CdSe/CdZnS core/shell quantum dots into a silica shell around preformed silica microspheres. This nanocomposite is used in real-time targeting fluorescence microscopy imaging for blood vessels through guidance of external magnetic field.¹⁵ Further to this, Klimov et al. had successfully synthesized Co NCs overcoated with a layer of CdSe that possess ferromagnetic properties in the core while exhibiting luminescent optical properties in the shell, which are useful as labels or tags in specific targeting biological labeling.¹⁶

* Corresponding author. Tel.: +6(019) 3292772, +6(03) 89248601. Fax: +6(03) 89248017. E-mail: WEE-SIONG.CHIU@nottingham.edu.my.

[†] University of Nottingham Malaysia Campus.

[‡] University of Malaya.

[§] Universiti Kebangsaan Malaysia.

Up to this date there are few examples of truly bifunctional behaviors (coexistence of magnetic and optical properties) through core-shell engineering. As compared to the successful preparation of oxide-supported metal nanoparticles using the method consisting of chemo-physical blending or electrostatic stabilization mechanisms,^{17,18} the development of magnetic/semiconductor core-shell NCs as mentioned above remains lagging behind. This could be attributed to the difficulty in creating a reaction condition, which enables the overgrowth of one material over the other through appropriate lattice mismatch.⁸ Furthermore, most of the crystal systems for oxide-based magnetic materials (which are stable during reaction) exist in a cubic system, while oxide-based semiconductor materials exist in a hexagonal system. The large variation in lattice parameter for these two crystal systems strictly promotes the formation of an alloy rather than an overgrowth process. Consequently, all these obstacles have limited the syntheses and studies of these truly bifunctional NCs. Hence, it is crucial to find a synthetic approach that is highly effective in preparing core-shell bifunctional NCs.

Hereby, we report a new type of bifunctional magnetic-semiconductor core/shell NCs, which were composed of magnetic metal oxide, Fe₃O₄, as the core and an oxide-semiconductor, ZnO, as the shell. The overgrowth of the ZnO layer was proceeded on the surface of Fe₃O₄ NCs via seed-mediated growth approach by rapid thermal decomposition of organometallic compound, zinc acetate (ZnAc). Although Fe₃O₄ (core) and ZnO (shell) exist in face-center-cubic and hexagonal crystal structures, respectively, current approach has shown the feasibility in growing the core-shell NCs with different crystal structures, while instances of core-shell NCs with different crystal structures remain rare. As a comparison with the preceding report, there is not interdiffusion of the elements between core and shell that subsequently caused the formation of an alloy.^{19–21} Moreover, current approach can produce highly crystalline core-shell NCs with narrow sizes and shapes distribution and show no tendency to aggregate compared to preceding reports.^{22,23}

Experimental Section

All the chemicals were used without further purification. Fe₃O₄/ZnO core/shell NCs are prepared by two-step process, whereby the first step involved the preparation of stock solution for Fe₃O₄ NCs (employed as seeds) and shell precursor, respectively, while the second step involves the overgrowth of ZnO on the surface of Fe₃O₄ NCs.

Preparing the Stock Solution for Fe₃O₄ NCs. Fe₃O₄ NCs were synthesized in our previous work.²⁴ The as-synthesized Fe₃O₄ NCs that have been dispersed in *n*-hexane was loaded into a 250 mL four-neck flask, which contained pyridine, and heated to 60 °C for 30 min under vacuum. The heating process was controlled by a digital temperature controller (JKEM-Model 310) equipped with a PID system that avoids temperature overshoot and provides the best sensitivity. During heating, the mixture was evacuated repeatedly with the assistance of a mechanical pump to remove *n*-hexane. After the *n*-hexane was fully eliminated, the dispersion of Fe₃O₄ NCs in pyridine was refluxed for 8 h at 117 °C under continuous purge with Ar gas. During reflux, pyridine displaced oleic acid from the Fe₃O₄ NCs surface and subsequently formed a labile bond on its surface, making Fe₃O₄ NCs more accessible to the surface and amenable to the shell growth. After reflux, the sample was transferred into test tubes and *n*-hexane was added followed by centrifugation to remove excessive oleic acid. The precipitate was

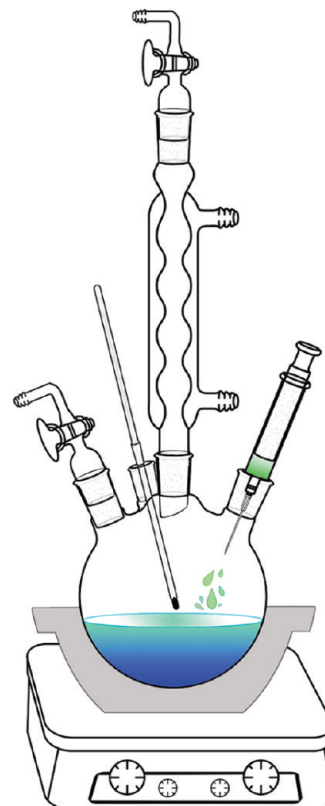


Figure 1. Representation of the synthetic apparatus setup for the preparation of Fe₃O₄/ZnO core/shell NCs.

redispersed in *n*-hexane before reprecipitated by adding excessive ethanol. The process of dispersing and precipitating was repeated three times. Finally, the precipitates were dissolved in *n*-hexane and were ready to be used as a stock solution with a concentration of 1.67×10^{-5} mol/mL for the overgrowth of ZnO shell.

Preparing the Stock Solution of ZnAc. ZnAc (0.01 mol; Zn(CH₃CO₂)₂, Aldrich, ≥99.99%) was loaded into a 250 mL four-neck flask in which contained 100 mL of *n*-octadecene. The mixture was heated to 80 °C under a flow of Ar gas with robust stirring for 1 h. Meanwhile, the mechanical pump was used to evacuate the residual amount of water with regular intervals of 15 min. Finally, the mixture was cooled down to room temperature and stored under N₂ in the refrigerator as stock solution.

Synthesis of Fe₃O₄/ZnO Core/Shell NCs. The apparatus setup for synthesis of Fe₃O₄/ZnO core/shell NCs is depicted in Figure 1. A total of 60 mL of the stock solution of Fe₃O₄ NCs together with 80 mL of *n*-octadecene were poured into a 250 mL four-neck flask, equipped with an Allihn condenser and heated to 100 °C for 30 min under vigorous magnetic stirring. The mixture was repeatedly evacuated with a mechanical pump to remove *n*-hexane and residual amount of water. Then the mixture was ramped to 317 °C (with constant heating rate of 25 °C/min), and 10 mL of ZnAc stock solution was injected dropwise (1 drop per second) scrupulously through a syringe pump into the reaction solution. The mixture was refluxed at this temperature under continuous purge of Ar gas. The mole ratio of Fe₃O₄ NCs to ZnAc was equal to 1:1 for this sample (denoted as sample A afterward). Upon injection, the gas evolved on the top of the mixture, which implies the decomposition of ZnAc and, subsequently, formation of a ZnO shell on the surface of Fe₃O₄ NCs occurred. Further annealing through refluxing is required to trigger atomic diffusion to the correct

position for developing into well-ordered crystals lattice. After 2 h, $\text{Fe}_3\text{O}_4/\text{ZnO}$ core/shell NCs were isolated from solvents and unreacted reagents by centrifugation with the combination of ethanol and *n*-hexane. Finally, the precipitates were dried in a vacuum desiccator overnight. Similar procedure was repeated to prepare sample B, with mole ratio of Fe_3O_4 NCs to ZnAc equal to 2:1.

Characterization. The morphologies of $\text{Fe}_3\text{O}_4/\text{ZnO}$ core/shell NCs were characterized by transmission electron microscope (TEM; Philips CM12 with operation voltage 100 kV). After the images were digitized, NC diameter and size distribution analysis were carried out using I-Solution-DT (version 6.5, IMT) software with at least 500 NCs being chosen as the sampling data. To identify the crystal structures as well as the composition of the samples, X-ray diffractometer (X'PERT PRO PW3040, Cu K α radiation, and wavelength, $\lambda = 0.154$ nm) was employed with a scanning rate of $0.01^\circ/\text{s}$. Energy-dispersive X-ray (EDX) spectrometry using a field-emission scanning electron microscope (FESEM LEO SUPRA 55VP, operation voltage 15 keV) operating in scanning mode was used to confirm the alloy-free composition by directing the electron beam onto a single NC. Vibrating sample magnetometer (VSM, Lakeshore 736–7400 Series, equipped with integrated gaussmeter) was used to measure the magnetic properties. A UV–visible spectrophotometer (Varian Cary 50) equipped with a xenon flash lamp for best sensitivity, which reduces excessive photometric noise filtration, was used for monitoring the absorption peak of $\text{Fe}_3\text{O}_4/\text{ZnO}$ core/shell NCs.

Results and Discussion

Figure 2 shows a series of low and high magnification TEM micrographs for the as-synthesized Fe_3O_4 NCs and $\text{Fe}_3\text{O}_4/\text{ZnO}$ core/shell NCs. For all the TEM micrographs, the magnification power had been standardized with identical magnification, respectively, for both low magnification ($45000\times$) and high magnification ($430000\times$) to further elucidate the formation of core–shell structures, which is distinctive from their parental seeds. As depicted in Figure 2a, all the Fe_3O_4 NCs that have been refluxed for 8 h are spherical in shape and highly monodispersed. Additionally, there are no agglomerations observed between NCs, and the mean diameter of these Fe_3O_4 NCs lies within the range of 8–13 nm. According to the high-magnification TEM image (Figure 2b), the lattice fringes with a high degree of extended structural ordering for these Fe_3O_4 NCs are clearly seen, which implies the fully crystalline structure. These Fe_3O_4 NCs have been used in a seed-mediated grow approach to overgrow a layer of ZnO on its surfaces.

Figure 2c depicts the as-synthesized $\text{Fe}_3\text{O}_4/\text{ZnO}$ core/shell NCs (sample A). Typically, all these NCs remain spherical in shape similar to their parental-seeds and preserve its monodispersity. However, the average diameter of this core/shell NCs are somewhat larger than those of the cores and the average diameter lies in the range of 17–19 nm. The average thickness of the shell-layer is determined to be about 4.45–5.15 nm. As shown in the micrograph, the core of all the core/shell NCs appears to be with darker dots if compared to the shell due to the difference in electron scattering power when the electron beam strikes on its surface. This is attributed to the higher electron density of Fe_3O_4 NCs (core), which gives more contrast than ZnO (shell) because the shell layer has fewer electrons per unit cell.²⁵ Meanwhile, the random speckled backgrounds are also observed in this figure, which could be due to the backscattering of electron beams after it struck the amorphous carbon substrate.

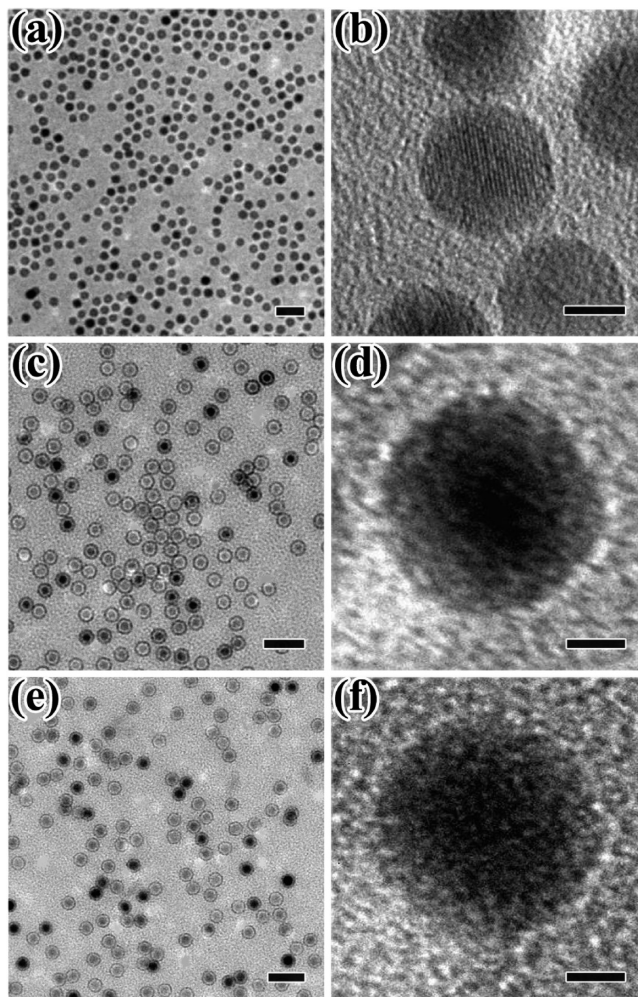


Figure 2. TEM micrographs of (a,b) Fe_3O_4 NCs being employed as seed, (c,d) $\text{Fe}_3\text{O}_4/\text{ZnO}$ core/shell NCs synthesized with a mole ratio of Fe_3O_4 NCs to ZnAc equal to 1:1 (sample A), (e,f) $\text{Fe}_3\text{O}_4/\text{ZnO}$ core/shell NCs synthesized with a mole ratio of Fe_3O_4 NCs to ZnAc equal to 2:1 (sample B). The magnification for (a), (c), and (e) is $45000\times$, with a scale bar of 40 nm, while the magnification for (b), (d), and (f) is $430000\times$, with a scale bar of 4 nm.

The growth of the ZnO shell proceeded through heterogeneous nucleation rather than forming separate nuclei by homogeneous nucleation. This is attributed to the presence of Fe_3O_4 NCs that play the role as seeds to create a condition of lower activation energy in promoting heterogeneous nucleation rather than homogeneous nucleation.²⁶ As long as the homogeneous nucleation is bypassed by the presence of the seeds, all the undergoing overgrowths are taking place at almost identical growth conditions. Thus, the overall diameters of NCs are maintained at narrow size distribution during their evolution with standard deviation of $\pm 4\%$. The high-magnification TEM image in Figure 2d further affirms the formation of the core/shell structure. The core diameter is determined to be about 8.3 nm, and this value is well-correlated with the diameter of its parental seed in Figure 2b with the same magnification. However, the lattice fringes are not clearly observed along its surface due to the formation of a polycrystalline shell. Hence, it is deduced that the overgrowth was initialized by a random and highly nonepitaxial nucleation process of ZnO on the surface of Fe_3O_4 NCs followed by ZnO particle growth and nanocrystalline merging.

When the mole ratio of Fe_3O_4 NCs to ZnAc was increased from 1:1 to 2:1 (sample B), there is not much variation from

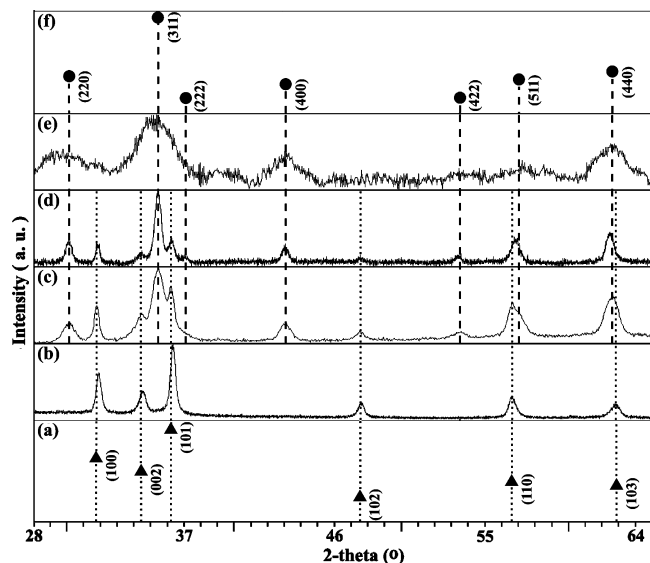


Figure 3. XRD patterns for the (a) standard pattern of ZnO (JCPDF: 00-036-1451), (b) ZnO NCs, (c) Fe₃O₄/ZnO core/shell NCs (sample A), (d) Fe₃O₄/ZnO core/shell NCs (sample B), (e) Fe₃O₄ NCs, and (f) standard pattern of Fe₃O₄ (JCPDF: 01-075-0033).

the aspect of morphologies as compared to sample A (Figure 2e). However, a slight decrease in average diameter is observed, where the average diameter lies within the range of 15–18 nm. The shell thickness is determined to be within the range of 3.0–4.5 nm. The decrease of shell thicknesses is due to the high concentration of Fe₃O₄ NCs that present during the overgrowing process. During heterogeneous nucleation that occurred under a high concentration of seed material, the ZnAc precursor was distributed equally among the Fe₃O₄ NCs that were twice the concentration as compared to sample A. Hence, lower shell thickness formed and subsequently reduced the overall diameter of NCs in sample B. This is agreed well with the LaMer model that emphasized controlled growth through consuming an equal amount of feedstock by preformed nuclei, which is a slow and long process to produce highly monodisperse colloidal particles.²⁷ As it is shown in the high-magnification TEM image for the selected NCs from sample B (Figure 2f), the thickness of the shell appears to be less, compared to sample A (Figure 2d). Apparently, there is a loss of contrast across the outer layer, particularly noticeable along the bottom-left, which suggests the presence of a much thinner ZnO shell than that of the stronger scattering Fe₃O₄ core.

Figure 3 shows a series of X-ray diffraction (XRD) patterns for various NC samples consisting of ZnO, Fe₃O₄/ZnO core/shell, and Fe₃O₄, together with their standard patterns. Upon shell growth, the spectra and relative intensities for both sample A and sample B (Figure 3c and d) are systematically well-correlated with the spectra of their counterparts in single-component constituted ZnO (Figure 3b) and Fe₃O₄ NCs (Figure 3e). Apparently, both of the spectra of these single-constituents can be well indexed to the standard patterns of ZnO (Figure 3a, which is a hexagonal phase) and Fe₃O₄ (Figure 3f, which is a face-center-cubic phase). This suggested that the shell growths for both sample A and sample B yield a crystalline shell without alloying, because it has been confirmed²⁸ that homogeneous alloying can cause obvious shifts in the diffraction patterns. Meanwhile, it is observed that the broadening peaks due to the finite size effect in the diffraction pattern of the Fe₃O₄ core alone (Figure 3e) are compensated by the narrower peaks, as indicated in the diffraction patterns of both sample A and sample B. These narrower peaks, which are assigned to the Fe₃O₄ core, imply

the formation of larger crystallite size due to the formation of more profound crystalline structure as the result of extended annealing duration for 2 h during overgrowth process. By increasing the mole ratio of Fe₃O₄ NCs to ZnAc from 1:1 (sample A) to 2:1 (sample B) during the overgrowth process, the relative intensities of all the peaks for ZnO decrease (Figure 3d) if compared to sample A (Figure 3c). This implies that a lesser amount of ZnO had deposited on the surface of the core (Fe₃O₄ NCs) to form a shell layer, and this deduction is well-complemented with the TEM micrograph for sample B (Figure 2e), where a slight decrease in the shell thickness had been observed.

Figure 4 depicts a representative EDXA spectrum for sample A. According to the spectrum, the sample composed of Fe, Zn, O, C, and Cu. No other additional elements are present except for the peak assigned to C, which is attributed to the residual surfactant molecules that were adsorbed on the surface of the NCs, whereas the Cu peak is originated from carbon coated copper grid. This spectrum is well-complemented with the XRD measurements, which shows that most of the ZnAc constituents were successfully removed from the NCs as there is no additional diffraction peaks assigned to ZnAc precursor in XRD pattern.

Figure 5 shows magnetization curves for samples A and B. Typically, both of the samples exhibit superparamagnetic properties, where no coercivity are observed and the magnetic moments are only induced in the presence of magnetic field. Upon removal of the magnetic field, the induced nonpermanent dipoles diminished due to the disruption of net magnetic moments by thermal energy. Both of the samples show the ease in magnetization due to high susceptibilities, where magnetic field approximate 1800 kOe is sufficient to induce 82% of the total magnetization. As a comparison, the saturation magnetization for sample B (30.0 emu/g) is higher than sample A (12.0 emu/g) due to the higher percentage of Fe₃O₄ NCs present in sample B that caused it to have higher magnetic moment. However, the saturation magnetizations for both of the samples are lower if compared to bulk-size value (92 emu/g).²⁹ As reported by Zhang et al.,³⁰ the saturation magnetization as well as the magnetic moment of the particle is proportional to its size. Hence, bulk-size Fe₃O₄ renders higher saturation magnetization if compared to the as-synthesized Fe₃O₄/ZnO NCs.

Superparamagnetism NCs is beneficial in the formation of stable colloidal suspension that is highly dispersible in aqueous due to low tendency in interparticles agglomeration caused by dipole–dipole interaction if compared to that of permanent ferro- or ferrimagnetic NCs.³¹ Therefore, an irreversible magnetic interaction can be avoided and the abundant surface area is preserved. This is greatly assisted in heterogeneous catalytic reactions that normally influenced by interfacial electron transfer process between catalyst and the targeted reactants. Hence, the as-synthesized Fe₃O₄/ZnO core/shell NCs can become a good candidate to be used as a regenerable and reusable smart magnetic catalyst, which retains its surface area and requires a low-field magnetic separation.

Figure 6 illustrates the evolution of the room temperature optical spectral for various samples with identical concentration (28.57 ppm). The absorption cutoff wavelength for ZnO NCs is determined to be about 400 nm (Figure 6a). For Fe₃O₄ NCs, there is no obvious optical absorption observed (Figure 6b) because Fe₃O₄ is an indirect bandgap semiconductor, where its optical property is dominated by a broad featureless absorption tail characteristic.³² Additionally, Fe₃O₄ has been categorized as a weak semiconductor due to its narrow bandgap energy, E_g

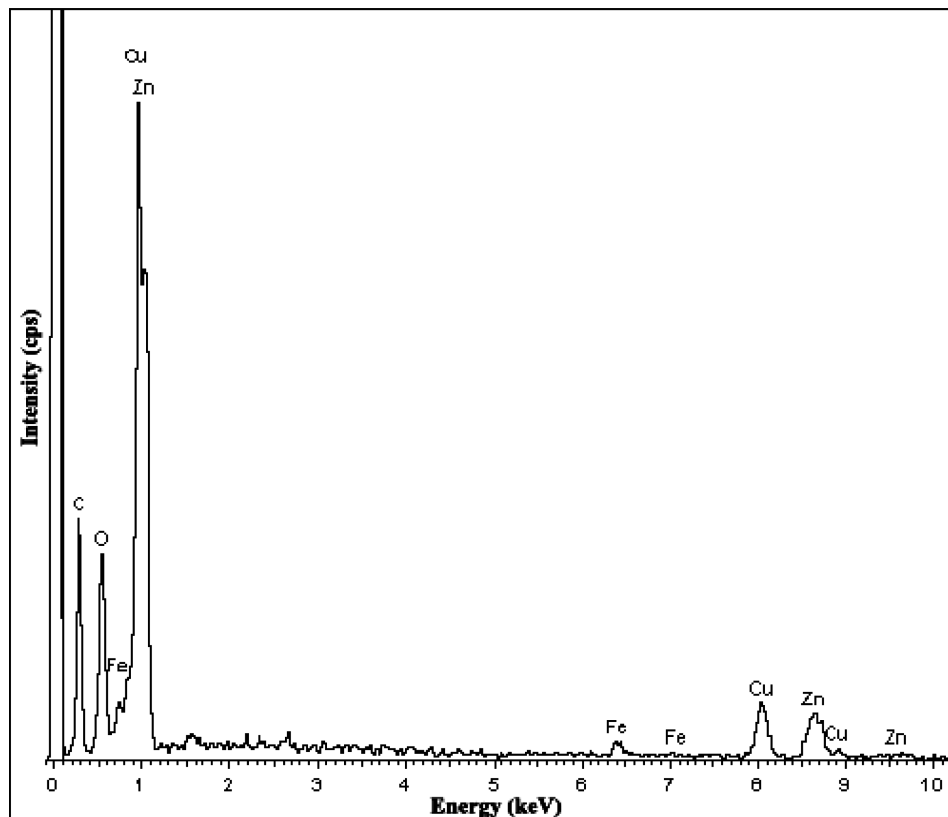


Figure 4. EDXA spectrum of sample A obtained by directing the electron beam onto a single NC.

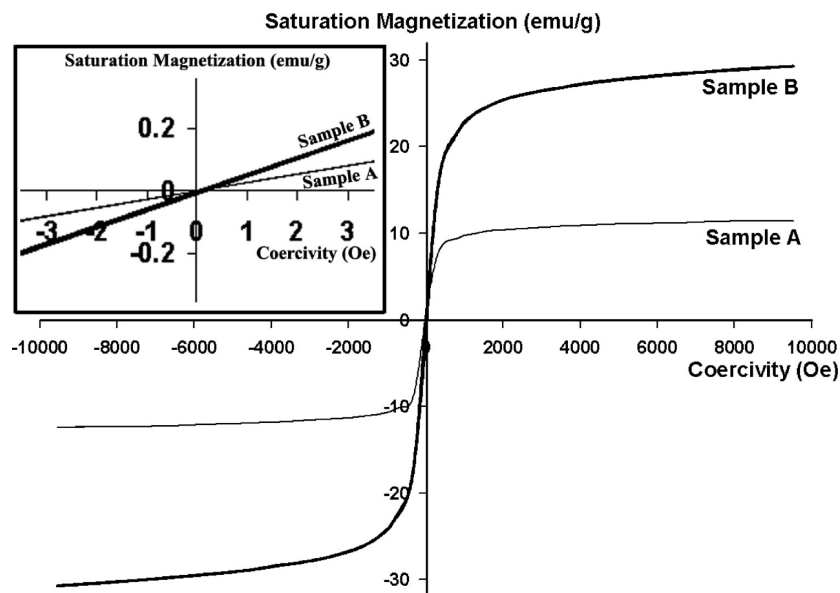


Figure 5. Magnetization curves measured at room temperature for samples A and B (inset: the intercept of the curves at origin shown that both of the samples are superparamagnetic with zero-coercivity).

(0.14 eV). This low bandgap energy causes its electrons or holes to have very low mobility which is due to the narrowness of *d*-bands that do not appreciably overlap.³³ Therefore, Fe₃O₄ exhibits an almost metallic nature where only negligible absorption is observed.

After overgrowing a layer of ZnO on the surface of Fe₃O₄ NCs (sample A), the absorption cutoff wavelength shows significant red-shift to the wavelength of approximately 500 nm (Figure 6b), suggesting that the present sample can absorb visible light within the wavelength of 400–500 nm. This could be attributed to the creation of interactive straining between core

and shell that alters their respective properties. The straining effect is caused by large variation in lattice parameters between core and shell, where all the lattice parameters values for ZnO (*a*, *b* = 3.2498 Å, *c* = 5.2066 Å) are smaller than those of Fe₃O₄ (*a*, *b*, *c* = 8.384 Å). As a result, the lattice mismatch occurs, where the core is subjected to the compressive force, while the shell is experiencing tensile strain. Both of these strain effects work in a concerted fashion that leads to the shifting of the bandgap energy to the red region of the spectra.^{12,34,35} Additionally, the red-shift phenomenon in the absorption spectra of the core/shell NCs in relation to that of ZnO alone is also an

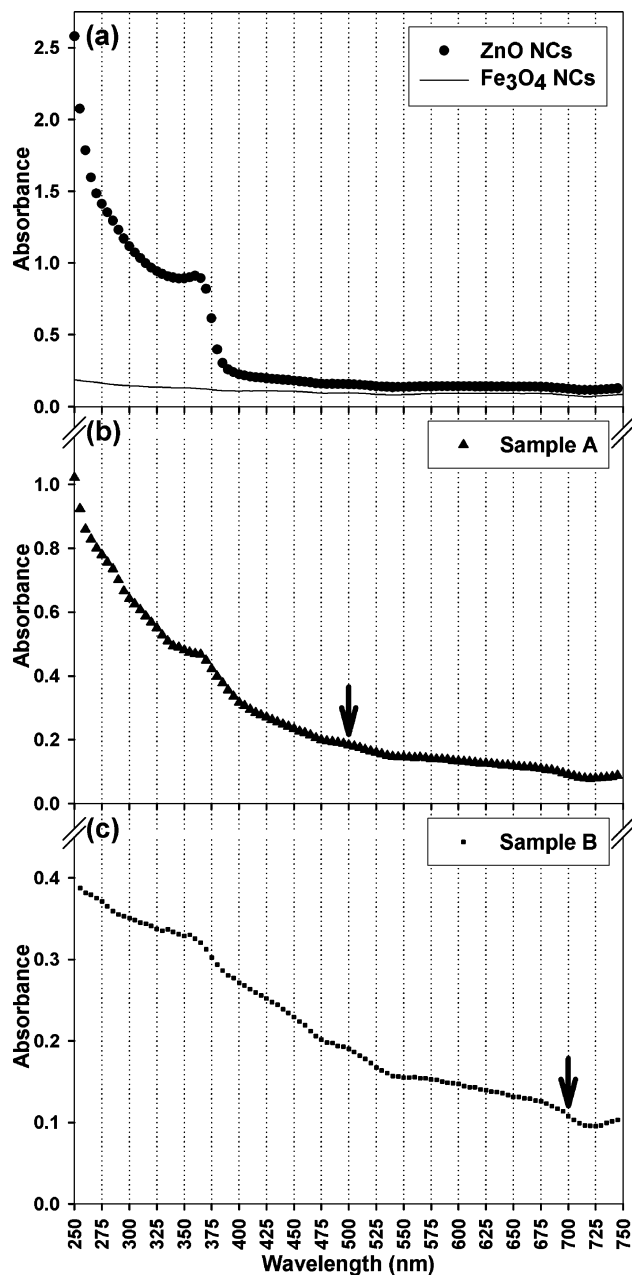


Figure 6. Room temperature optical absorption spectra for (a) ZnO NCs and Fe₃O₄ NCs, (b) sample A, and (c) sample B (arrows indicate the absorption cutoff wavelength).

indication of the formation of the core/shell structure. Several reports had shown that upon shell growth of a material with larger bandgap energy onto another of lower bandgap energy strictly promote this phenomenon.^{36,37} Hence, the possibility of alloying during shell growth can be discounted.

Meanwhile, for sample B, the absorption cutoff wavelength is found to shift to a higher wavelength approximating 700 nm (Figure 6c) if compared to that of sample A. The red-shift phenomenon could be due to the thinner ZnO layer on this sample if compared to sample A. The shell layer for this sample experiences higher tensile strain that distributes over a large fraction of the constituent atoms to form a homogeneous strain, while the core is under a strain-relaxing condition due to the negligible compressive force of thinner shell if compared to the thicker shell in sample A. Thus, the synergistic effect between the core and the shell is lower. As a result, the electronic energy gap strictly increases for the shell layer and this effect has been experimentally observed and theoretically predicted, where overgrowing a very thin shell consisting of a single monolayer can greatly result in the enlargement of the bandgap energy.^{38,39}

Figure 7 demonstrates the daylight pictures for magnetically induced separation of Fe₃O₄/ZnO core/shell NCs (sample A) by exploiting their magnetic property. A total of 0.05 g of sample A was dispersed in deionized water prior to sonication, and the dispersion appears to be brownish in color due to the formation of a suspension (Figure 7a). Upon placing the vial near to a magnet with a magnetic field of 0.6 T for 1 min, the progressive separation of a colloidal suspension is observed, where the suspension is attracted toward the wall of the vial that is closer to the magnet (Figure 7b). With increasing time duration to 2 min, the turbidity of the solution becomes increasingly discolored and finally becomes clear (Figure 7c), which implies the complete physical separation. Hence, this sample has the potential to be used as a bifunctional catalyst such as in the Fischer–Tropsch synthesis of hydrocarbons^{40,41} and for the metal-enhanced charge carrier delocalization materials.^{42,43}

Conclusion

In summary, we have developed a truly new type of bifunctional inorganic oxide-based Fe₃O₄/ZnO core/shell NCs that combine the magnetic and optical properties for the first time in a core/shell arrangement. The material composition and stoichiometry, as well as its magnetic and optical properties, have been examined and verified by various characterization techniques. Further studies are undertaken by using these NCs as regenerable and recycleable photocatalyst nanomaterials for the photodecomposition of organic-dye compounds. Finally, the efforts in investigating the effect of magnetic interactions on the rates of electron and hole recombination are also under pursued.

Acknowledgment. This project was supported by MOSTI under e-sciencefund (Project No. 03-02-12-SF0019), technofund (Project No. TF0106D212), and IRPA research grant (Project No. 09-02-02-0032-SR0004/04-04). W.S.C. thanks

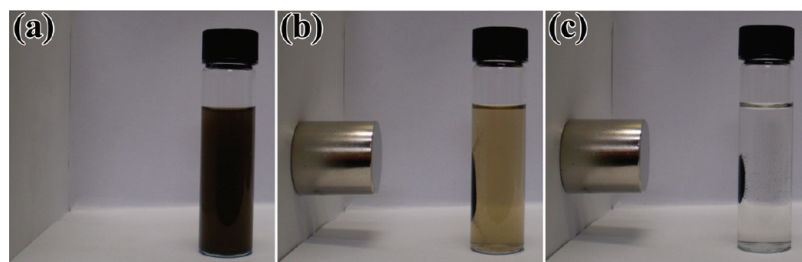


Figure 7. Daylight pictures for progressive separation of Fe₃O₄/ZnO core/shell NCs (sample A) from their original solution (a) without any magnetic field presence, (b) upon application of a 0.6 T magnetic field for 1 min, and (c) upon application of a 0.6 T magnetic field for 2 min.

Faculty of Engineering (University of Nottingham Malaysia Campus) for the Research Assistant Fellowship. The authors also gratefully acknowledge Normalawati Bt. Shamsudin, Suhaniza Bt. Razali, Ahmad Zaki B. Zaini, and Idris Sharif from the Electron Microscopy Unit (UKM) for their assistance in the TEM characterization. Finally, the authors thank K. N. Wong (UKM) for inspiring discussions and fruitful advice.

References and Notes

- (1) Formo, E.; Lee, E.; Campbell, D.; Xia, Y. *Nano Lett.* **2008**, *8*, 668.
- (2) Habas, S. E.; Lee, H.; Radmilovic, V.; Somorjai, G. A.; Yang, P. *Nat. Mater.* **2007**, *6*, 692.
- (3) Joo, S. H.; Park, J. Y.; Tsung, C.-K.; Yamada, Y.; Yang, P.; Somorjai, G. A. *Nat. Mater.* **2009**, *8*, 126.
- (4) Chiu, W. S.; Khiew, P. S.; Cloke, M.; Isa, D.; Tan, T. K.; Radiman, S.; Abd-Shukor, R.; Hamid, M. A. A.; Huang, N. M.; Lim, H. N.; Chia, C. H. *Chem. Eng. J.* **2010**, *158*, 345.
- (5) Gu, H.; Yang, Z.; Gao, J.; Chang, C. K.; Xu, B. *J. Am. Chem. Soc.* **2004**, *127*, 34.
- (6) Chiu, W. S.; Khiew, P. S.; Isa, D.; Cloke, M.; Radiman, S.; Abd-Shukor, R.; Abdullah, M. H.; Huang, N. M. *Chem. Eng. J.* **2008**, *142*, 337.
- (7) Cozzoli, P. D.; Manna, L. *Nat. Mater.* **2005**, *4*, 801.
- (8) Buonsanti, R.; Grillo, V.; Carlino, E.; Giannini, C.; Curri, M. L.; Innocenti, C.; Sangregorio, C.; Achterhold, K.; Parak, F. G.; Agostiano, A.; Cozzoli, P. D. *J. Am. Chem. Soc.* **2006**, *128*, 16953.
- (9) Casavola, M.; Grillo, V.; Carlino, E.; Giannini, C.; Gozzo, F.; Fernandez Pinel, E.; Garcia, M. A.; Manna, L.; Cingolani, R.; Cozzoli, P. D. *Nano Lett.* **2007**, *7*, 1386.
- (10) Peng, X. G.; Schlamp, M. C.; Kadavanich, A. V.; Alivisatos, A. P. *J. Am. Chem. Soc.* **1997**, *119*, 7019.
- (11) Schlamp, M. C.; Peng, X. G.; Alivisatos, A. P. *J. Appl. Phys.* **1997**, *82*, 5837.
- (12) Smith, A. M.; Mohs, A. M.; Nie, S. *Nat. Nanotechnol.* **2009**, *4*, 56.
- (13) Gao, X. H.; Cui, Y. Y.; Levenson, R. M.; Chung, L. W. K.; Nie, S. M. *Nat. Biotechnol.* **2004**, *22*, 969.
- (14) Masala, O.; Seshadri, R. *J. Am. Chem. Soc.* **2005**, *127*, 9354.
- (15) Insin, N.; Tracy, J. B.; Lee, H.; Zimmer, J. P.; Westervelt, R. M.; Bawendi, M. G. *ACS Nano* **2008**, *2*, 197.
- (16) Kim, H.; Achermann, M.; Balet, L. P.; Hollingsworth, J. A.; Klimov, V. I. *J. Am. Chem. Soc.* **2005**, *127*, 544.
- (17) Yan, W.; Mahurin, S. M.; Pan, Z.; Overbury, S. H.; Dai, S. *J. Am. Chem. Soc.* **2005**, *127*, 10480.
- (18) Zheng, N.; Stucky, G. D. *J. Am. Chem. Soc.* **2006**, *128*, 14278.
- (19) Halsall, M. P.; Nicholls, J. E.; Davies, J. J.; Cockayne, B.; Wright, P. J.; Cullis, A. G. *Semicond. Sci. Technol.* **1988**, *3*, 1126.
- (20) Hocheppied, J. F.; Bonville, P.; Pileni, M. P. *J. Phys. Chem. B* **2000**, *104*, 905.
- (21) Parbrook, P. J.; Wright, P. J.; Cockayne, B.; Cullis, A. G.; Henderson, B.; Odonnell, K. P. *J. Cryst. Growth* **1990**, *106*, 503.
- (22) Gui Huan, D.; et al. *Nanotechnology* **2006**, *17*, 2850.
- (23) Wan, J.; Li, H.; Chen, K. *Mater. Chem. Phys.* **2009**, *114*, 30.
- (24) Chiu, W. S.; Radiman, S.; Abdullah, M. H.; Khiew, P. S.; Huang, N. M.; Abd-Shukor, R. *Mater. Chem. Phys.* **2007**, *106*, 231.
- (25) Mews, A.; Kadavanich, A. V.; Banin, U.; Alivisatos, A. P. *Phys. Rev. B* **1996**, *53*, R13242.
- (26) Markov, I. V. *Crystal Growth for Beginners: Fundamentals of Nucleation, Crystal Growth and Epitaxy*; World Scientific: Singapore, 1995.
- (27) Lamer, V. K.; Dinegar, R. H. *J. Am. Chem. Soc.* **1950**, *72*, 4847.
- (28) Chiu, W. S.; Radiman, S.; Abd-Shukor, R.; Abdullah, M. H.; Khiew, P. S. *J. Alloys Compd.* **2008**, *459*, 291.
- (29) Jia, C. J.; Sun, L. D.; Luo, F.; Han, X. D.; Heyderman, L. J.; Yan, Z. G.; Yan, C. H.; Zheng, K.; Zhang, Z.; Takano, M.; Hayashi, N.; Eltschka, M.; Klau, M.; Rudiger, U.; Kasama, T.; Cervera-Gontard, L.; Dunin-Borkowski, R. E.; Tzvetkov, G.; Raabe, J. *J. Am. Chem. Soc.* **2008**, *130*, 16968.
- (30) Song, O.; Zhang, Z. J. *J. Am. Chem. Soc.* **2004**, *126*, 6164.
- (31) Leslie-Pelecky, D. L.; Rieke, R. D. *Chem. Mater.* **1996**, *8*, 1770.
- (32) Park, S. K.; Ishikawa, T.; Tokura, Y. *Phys. Rev. B* **1998**, *58*, 3717.
- (33) Matsumoto, Y. *J. Solid State Chem.* **1996**, *126*, 227.
- (34) Li, Y. H.; Gong, X. G.; Wei, S. H. *Phys. Rev. B* **2006**, *73*.
- (35) Maki, H.; Sato, T.; Ishibashi, K. *Nano Lett.* **2007**, *7*, 890.
- (36) Danek, M.; Jensen, K. F.; Murray, C. B.; Bawendi, M. G. *Chem. Mater.* **1996**, *8*, 173.
- (37) Talapin, D. V.; Nelson, J. H.; Shevchenko, E. V.; Aloni, S.; Sadtler, B.; Alivisatos, A. P. *Nano Lett.* **2007**, *7*, 2951.
- (38) Persson, J.; Hakanson, U.; Johansson, M. K. J.; Samuelson, L.; Pistol, M. E. *Phys. Rev. B* **2005**, *72*.
- (39) Wei, S. H.; Zunger, A. *Phys. Rev. B* **1999**, *60*, 5404.
- (40) Van der Laan, G. P.; Beenackers, A. *Catal. Rev.-Sci. Eng.* **1999**, *41*, 255.
- (41) van Steen, E.; Claeys, M.; Dry, M. E.; van de Loosdrecht, J.; Viljoen, E. L.; Visagie, J. L. *J. Phys. Chem. B* **2005**, *109*, 3575.
- (42) Cozzoli, P. D.; Fanizza, E.; Comparelli, R.; Curri, M. L.; Agostiano, A.; Laub, D. *J. Phys. Chem. B* **2004**, *108*, 9623.
- (43) Maeda, K.; Teramura, K.; Lu, D. L.; Saito, N.; Inoue, Y.; Domen, K. *Angew. Chem., Int. Ed.* **2006**, *45*, 7806.

JP100848M